ELSEVIER

Contents lists available at ScienceDirect

## **Applied Materials Today**

journal homepage: www.elsevier.com/locate/apmt



# Multiple concentric rainbows induced by microscale concave interfaces for reflective displays

Jacob Rada<sup>a,1</sup>, Haifeng Hu<sup>b,1</sup>, Lyu Zhou<sup>a</sup>, Jing Zeng<sup>c</sup>, Haomin Song<sup>a</sup>, Xie Zeng<sup>a</sup>, Shakil Shimul<sup>d</sup>, Wen Fan<sup>e</sup>, Qiwen Zhan<sup>b</sup>, Wei Li<sup>d</sup>, Limin Wu<sup>c</sup>, Qiaoqiang Gan<sup>a,\*</sup>

- <sup>a</sup> Department of Electrical Engineering, The State University of New York at Buffalo, Buffalo, NY 14260, USA
- b School of Optical-Electrical and Computer Engineering, University of Shanghai for Science and Technology, Shanghai 200093, China
- Eppartment of Materials Science and State Key Laboratory of Molecular Engineering of Polymers, Fudan University, Shanghai 200433, China
- <sup>d</sup> Department of Chemical Engineering, Texas Tech University, Lubbock, TX 79409, USA
- <sup>e</sup> Hubei Collaborative Innovation Center for Advanced Organic Chemical Materials, Ministry of Education Key Laboratory for the Green Preparation and Application of Functional Materials, School of Materials Science and Engineering, Hubei University, Wuhan, Hubei 430062, China

#### ARTICLE INFO

Article history: Received 14 July 2021 Accepted 1 August 2021

Keywords:
Microscale concave interface
Multiple concentric rainbow
Total interneal reflection
Optical interference
LIDAR
Autonamous systems

#### ABSTRACT

In our current world, active display technology creates a glut of energy demand to meet its illumination needs. This demand can be stymied by using reflective display technologies that require no active illumination, with some examples including: electronic paper using electrophoretic motion of ink particles, electrowetting of water/oil droplets, and interferometric modulators, all of which have been commercialized. However, due to the lack of active light sources, it is difficult to implement these reflective display technologies in low light environments (e.g. nighttime display). In this work, we report an experimental observation of multiple concentric circular rainbows from reflective microscale concave interfaces (MCIs), which are introduced by the reflection of optical rays within a polymer-embedded microsphere. Exit rays from a single edge and opposite edges will introduce completely different interference mechanisms depending on the illumination and observation conditions, which will result in different angledependent colors. By clarifying the mechanism behind this coloration phenomenon, as well as quantitatively mapping the generated color, the implementation of the MCI in smart signs and pixelated displays are demonstrated, showing angle-dependent color-changing reflected images that can be observed over a wide spatial angle range. This structural material will serve as a building block for the development of new platforms for light-matter interactions, on-chip sensors, anti-counterfeiting tools, and passive and smart color reflective displays. Intriguingly, we also demonstrate a smart MCI traffic sign for both visible and infrared wavelengths that will introduce extra signals for pattern and image recognition in order to enhance the safety of future autopilot/autonomous systems.

© 2021 Elsevier Ltd. All rights reserved.

## 1. Introduction

Display technology, as one of the most important branches of optoelectronics associated with modern life (e.g. televisions, smart phones, smart watches and glasses), has opened up huge markets along the way (e.g. electronic-paper [1–3], three-dimensional displays [4], virtual and augmented reality applications [5], electronic-skin display [6], etc.). However, as electronic/optoelectronic devices become more ubiquitous within our daily life, so too does the need to reduce the energy consumption of these devices, especially within display technologies. For instance, passive reflec-

E-mail address: qqgan@buffalo.edu (Q. Gan).

tive displays that rely on external light sources stand out because of their low energy consumption (e.g. e-paper, electronic-wetting [2] and MEMS interferometer displays [3]), especially when there is plenty of ambient light (such as sun light during the day). However, displays under low-light environments (e.g. nighttime outdoor display) still require active light emitting devices (e.g. LED displays), for example, nighttime advertisements and illuminated billboards on commercial streets and highways. In recent decades, global modernization and urbanization processes have increased the levels of ambient light pollution, enabling the use of nighttime satellite imagery to characterize the amount of regional development [7]. However, the increase in light pollution has also led to harmful impacts on ecosystems [8] and has even been affiliated with the spread of viruses [9] and cancers [10]. Therefore, a smart, passive display technology especially for nighttime use is essential

<sup>\*</sup> Corresponding author.

<sup>&</sup>lt;sup>1</sup> These authors contributed equally to this work.

for offsetting this ambient light pollution and its associated negative impacts on society. This article will report a new multiple concentric rainbow reflection from microscale concave interfaces (MCIs). By clarifying this new coloration mechanism and integrating these new structures with display components, we demonstrated a new reflective color display which is particularly useful in nighttime smart traffic signs and billboards on highways, reflective safety vests, anti-counterfeiting labels, entertainment toys, *etc.* 

Recently, a total internal reflection (TIR) interference mechanism introduced by MCIs was proposed [11] and enabled new optical microscopic imaging technologies [12]. However, it was believed that the incorporation of this new color creation mechanism into large scale displays and sensors is exciting but challenging to achieve [13]. Independently, a similar, but large-scale structure was realized by partially embedding a monolayer array of polymer microspheres into a transparent tape [14]. This structure was responsible for generating iridescent and vivid retroreflective colors, which was utilized as the building block for smart traffic signs [14,15]. Although both pioneering works [11,14] attributed the coloration mechanism to TIR (different from rainbow in nature [16,17]), neither work was able to definitively prove the exact nature of the color generation, which is essential for a color display application. In order to explain the physics of this reflective structural coloration strategy [11-15], it is necessary to introduce the key results reported by the pioneering works first.

Within Ref. [11], a multi-bouncing TIR model was proposed to explain the generated color (Fig. S1a in Section S1). When a beam of collimated light enters the microdroplets, it will experience many reflections within the droplet, due to the concave structure of the bottom surface. Furthermore, the beam will be split into different components, which will bounce a number of times, m, within the concave structure. Due to the different optical paths for m = 2, 3, 4 ..., an interference spectrum will be formed because of the constructive and destructive interference experienced by the beam components. Using this hypothesis, the TIR-induced spectral interference patterns were modeled analytically using ray optics and classical interference equations. In order to realize the color that is a result of a given spectrum, these interference patterns were then converted into a point on the Commission Internationale de l'Eclairage (CIE) color chart. However, colorimetric information does not have a one-to-one correspondence with the spectral feature of light. The same color found on the CIE chart can be a result of two totally different spectra (a concept known as metamerism [18]). Therefore, the utilization of the modeled color to definitively characterize the given sample should not be regarded as conclusive. On the other hand, within Ref. [14], a direct measurement of the reflected spectrum was obtained, but did not agree well with the multiple ray interference coupled from a single side of the microscale concave structure proposed by Ref. [11]. Instead, this work attributed the new color creation to thin-film interference introduced by an air gap between the microspheres and adhesive polyacrylate (i.e., the tape) interface (Fig. S1b in Section S1) [14]. However, the extracted air gap within the range of ~100 nm was not clearly observed in the microscopic characterization. Therefore, both reported mechanisms should be considered incomplete or inaccurate. In this work, we will begin by presenting a systematic experimental investigation to reveal the unambiguous complete mechanism for the colored reflection from the new MCI.

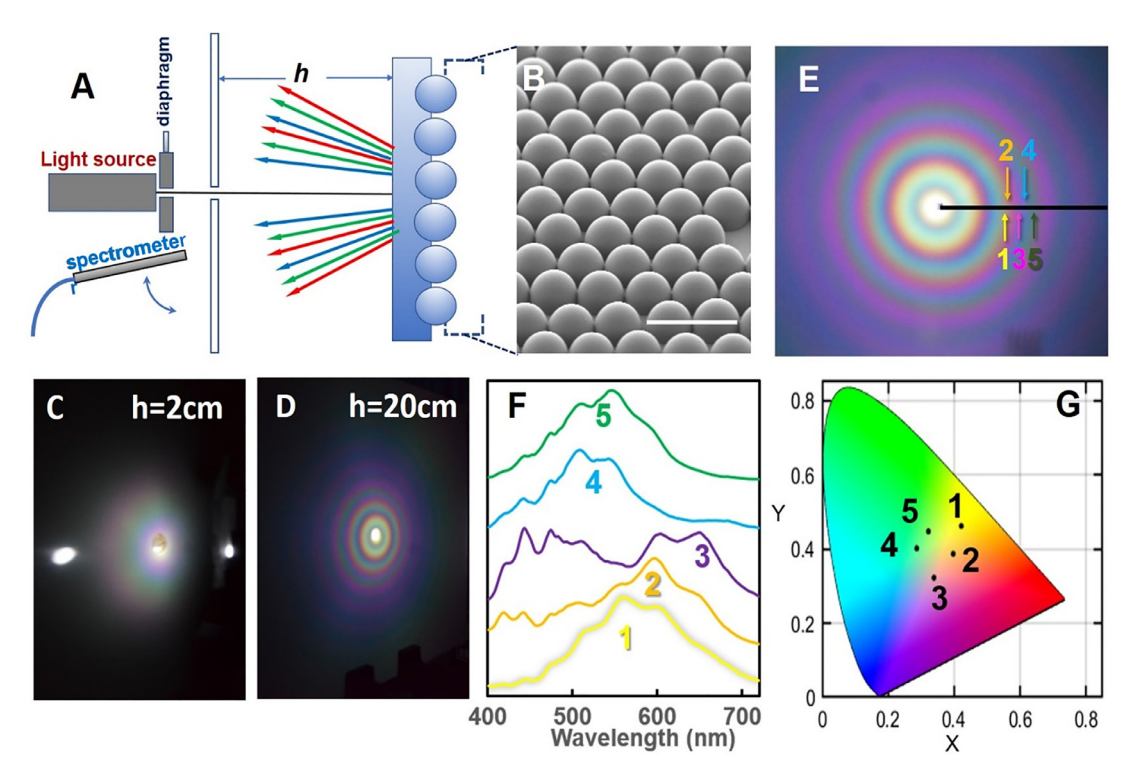
## 2. Results and discussion

Fig. 1**A** shows our experimental setup: A hetero-interface MCI sample with 10 μm polystyrene (PS) microspheres partially embedded in a tape substrate (Fig. 1**B**, see *Methods* for fabrication details of the MCI structure) was illuminated by a collimated beam through an optical diaphragm. The reflection from the illuminated

spot can be directly observed on a white board. As shown in Fig. 1C, when the distance between the MCI sample and the white board, h, was set at 2.0 cm, a colorful reflection was observed under the normal incidence. Intriguingly, when h was tuned to longer distances (see Supporting Video S1), a clear, multiple concentric rainbow pattern was observed (e.g. at 20.0 cm in Fig. 1D observed at an oblique angle). This unique rainbow ring pattern in the reflection side was not disclosed in the previous two pioneering works [11,14] and can provide an unambiguous explanation to the physics of this coloration phenomenon. To reveal the actual spectral feature of this multiple rainbow pattern (Fig. 1E observed at the normal direction at a distance of 30 cm), we then employed a fiber-based spectrometer to measure the angle dependent spectra. The spectrometer was pointed towards the center of the concentric rainbow pattern. For instance, raw data at five different angles are plotted in Fig. 1F (i.e., see arrows 1-5 in Fig. 1E, at output angles between 5.0° and 8.0°) and their corresponding colors in the CIE chart were plotted in Fig. 1G. The key question is whether these measured spectra and colors can be explained using recently proposed optical theory (e.g. [11] or [14]). If not, what was missing in previously reported works?

To begin with, we used a ray optics simulation software (Ray Optics module within COMSOL Multiphysics) to model the far-field feature of the reflected light. It should be noted that it is challenging to analyze the interference phenomenon using full wave methods since accurate modeling of TIR requires smooth surface of these microspheres. Considering the refractive indices of the tape ( $n_t = 1.47$ ) and the PS microsphere ( $n_s = 1.60$  [19] in our hetero-interface MCI structure, the optical path under the collimated normal incidence condition is remarkably clean: only m = 2and m = 3 are allowed in this hetero-tape/PS MCI structure (see details in Sec. S2 in the supplementary information). Higher order bouncing rays cannot be coupled into the sphere under normal incidence due to the deflection of the incident rays at the tape/sphere interface (see details in Sec. S3). Therefore, the refractive index distribution is one of the major differences compared with the homo-interface concave structure reported by Ref. [11]. In particular, the hetero-interface MCI structure is much easier to clarify the mechanism than the homo-interface structure that can support many higher orders bouncing rays. Another major difference is that Ref. [11] and its follow up work [20] mainly explained the interference coloration mechanism under a large incident angle (e.g. 40° to 50°). However, some experimental results under normal incidence were also provided in [11]. The important angle dependence of the proposed MCI structure was neglected (in Section S4, we show a detailed analysis of experimental data reported in the main text of Ref. [11] to reveal the inconsistency between the experimental observation and its proposed theory). As will be elucidated in this work, the multi-bouncing TIR picture is not an exclusive mechanism in this MCI structure. The interference mechanism will change significantly under different incident angles.

Angle dependence: As shown in Fig. 2A, under the normal incidence condition, the spatial angle ranges of the output rays with m=2 and m=3 are plotted by solid curves (using the modeling procedure outlined in Section S2, see Fig. S2b). Due to the geometric symmetry, the normal incident rays can enter the sphere from either right or left edges and propagate along the concave sphere/air interface via TIR along the clockwise or anti-clockwise directions, respectively (the range of their output angles  $\theta$  are plotted in Fig. 2A). The reflected light intensity in the far field is calculated by the superposition of different rays with the same output angle  $\theta$  (using Eqs. S1 and S2 in Section S2). Intriguingly, in this hetero-MCI structure, there exist two major superposition mechanisms for output rays. In the yellow shaded region in Fig. 2A (i.e.  $\pm 39.7^{\circ}$  to  $\pm 54.1^{\circ}$ ), there are only two exit rays from the same side of the sphere (i.e., m=2 and m=3 indicated by the same col-



**Fig. 1.** Far-field concentric rainbows from the MCI. (A) The experimental setup that allows for the concentric rainbow rings to be observed. A collimated white-light source is placed directly behind, and in the center of a white board, and illuminates the MCI sample. A spectrometer is employed to record several spectra at different angles. (B) SEM image of the embedded 10  $\mu$ m microspheres within the sticky polyacrylate tape (scale bar = 20  $\mu$ m). (C,D) Multiple concentric rainbow rings are observed by varying the MCI-white board distance, h at (C) 2 cm, and (D) 20 cm, respectively. (E) At a distance of h = 30 cm, the spectra of five separate points among the rings were measured using a fiber-based spectrometer (labeled 1–5 along the black axis). (F) The corresponding raw spectral data from the previously measured positions in (E). (G) The CIE points of the numbered measurement locations of (E).

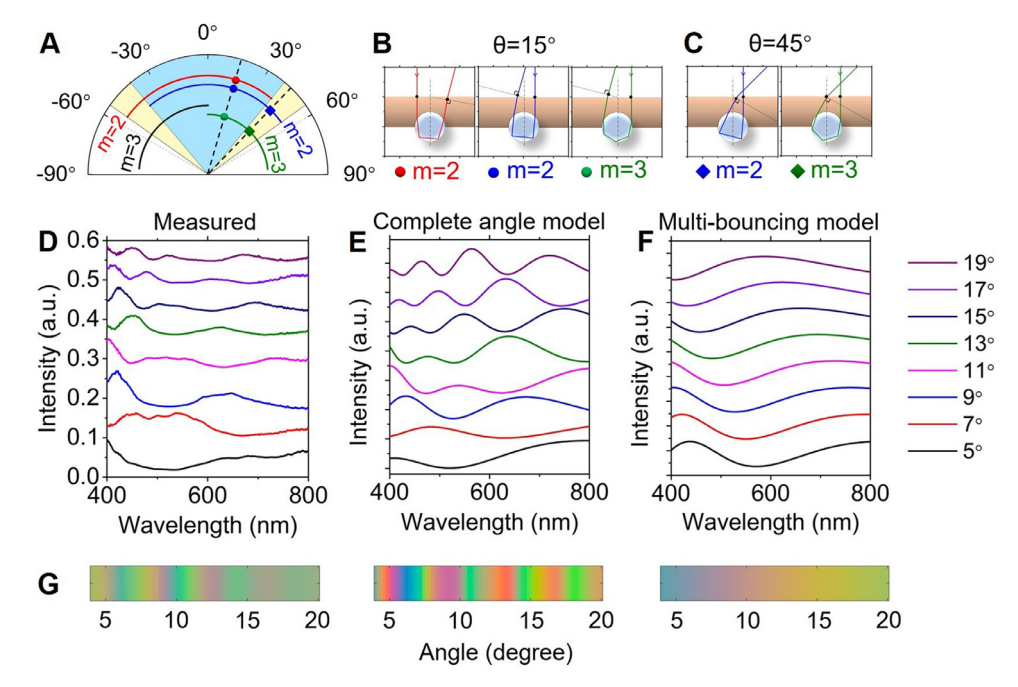


Fig. 2. Interference mechanism and reflective spectra of the MCI structure. (A) Modeled output angle ranges of the reflected rays experiencing different amounts of TIR. The solid curves represent the modeled angle ranges of the rays in the following cases: blue/red curve for clockwise/anti-clockwise propagating ray with m=2, and green/black curve for clockwise/anti-clockwise propagating ray with m=3. (B,C) Modeled trajectories of the light rays with an output angle of (B)  $\theta=45^\circ$ , and (C)  $15^\circ$ , respectively. (D) Measured angular spectra of the 10  $\mu$ m PS MCI sample in the far field (normalized by the incident light spectrum). (E-F) Simulated interference patterns in the far field by considering (E) the angle-dependent interference, and (F) the multi-bouncing interference method, respectively. (G) Modeled colors based on the measured raw spectra and modeled ones in (D-F) by considering the incident light spectrum. The measured and complete angle-dependent model spectra show colors being formed in a repetitive band, while the multi-bouncing model colors gradually change as the angle increases (For interpretation of the references to color in this figure legend, the reader is referred to the web version of this article.).

ored curves). For instance, when  $\theta$ =45° (as marked by the rectangles in Fig. 2A), only two optical paths can exist as shown by the ray tracing modeling results in Fig. 2B. This is the multi-bouncing TIR superposition proposed by Ref. [11]. According to the major experimental results reported in Refs. [11] and [20], the vivid colors were mostly observed under the incident angle of 40° to 50°. However, in the smaller output angle region (i.e., the blue shaded region between  $\pm 39.7^{\circ}$ ), the output rays from both sides of the sphere should be considered. For instance, at  $\theta$ =15° three rays exist as marked by the solid circles in Fig. 2A. Among these three rays shown in Fig. 2C, two of them both experience TIR twice, but enter and escape the sphere from the opposite edge (i.e., m = 2, see the left and central panels in Fig. 2C). They will also interfere with each other under given conditions. However, in Ref. [11], the underlying physical phenomenon that gave rise to the colors was attributed to the first mechanism only. The key assumption was described as: "this light exists at a distance farther than the coherent length of white light from the light propagating in the other direction". Ref. [11] claimed that they "do not expect interference between these two sets of trajectories". In other words, the superposition of exit rays from opposite edges of the sphere was excluded, which, unfortunately, misinterpreted the spatial coherent length of the light source. Next, we analyze the actual interference mechanism of the observed multiple concentric rainbows.

A complete angle-dependent interference mechanism: In order to determine if interference between two rays exiting the sphere at opposing edges is possible, the spatial coherent area of the light source is considered (i.e.,  $\Delta A \sim \frac{L_D^2 \tilde{\lambda}^2}{S}$ ) [21], which is determined by the distance between the light source and the MCI structure  $(L_D)$ , the mean wavelength of the incident light  $(\bar{\lambda})$ , and the emitting area of the light source (i.e., the opening area, S, of the diaphragm in Fig. 1A). One can see that it is not a fixed value when experimental conditions are tuned. For the white light sources used in our far-field experiment (i.e., a halogen lamp and a laser-driven white light), the transverse coherent length is at least  $95\sim144~\mu m$ (**Section S5**), which is larger than the diameter of spheres used in Refs. [11,14,20]. Therefore, the interference between two rays that exit the sphere on opposite edges cannot be ignored, especially under the illumination of a white light source of a microscope in the far-field [11] (see experimental characterization details in a microscope system in Section S5). Next, we will present experimental evidence to demonstrate this complete angle-dependent superposition by considering both interference mechanisms (i.e., the ray interference from opposite edges of the sphere and the multibouncing mechanism from a single side of the sphere). Specifically, we will analyze this phenomenon by comparing the spectral feature and spatial patterns, respectively.

Spectral features: Since the one-to-one correspondence between the spectral feature and the observed color was missing in Ref. [11], we will begin by characterizing the angle-dependent reflectance spectra within an angular range of 3° to 20° (8 spectra at selected angles are plotted in Fig. 2D). The corresponding spectra using complete angle-dependent interference and the exclusive multi-bouncing TIR interference are plotted in Fig. 2E and **F**, respectively. It is obvious that in the angle range from 5° to 19° the major feature of the measured spectra agreed well with those shown in Fig. 2E. In contrast, the modeled spectra that utilizes the multi-bouncing TIR interference mechanism [11] (Fig. 2F) did not show close correlation with the measured spectra. Therefore, the interference of two rays exiting from opposite edges of the sphere is a key component among the combined mechanisms in this small angle range. The measured and modeled angle-dependent reflectance spectra are then converted into colors that are perceptible to the human eye, and plotted in Fig. 2G. One can see that the multiple rainbow pattern can be reproduced only when the complete angle-dependent interference is considered, which is significantly different from the one produced by the exclusive multibouncing TIR interference picture. It should be noted that although one can see clear similarity between the measured spectra and the modeled ones, the color is still different (since the measured spectra are results of combined rays from symmetric positions on the ring, multi-bouncing TIR interference and the grating diffraction), further demonstrating that the direct color comparison cannot be used to definitively explain the resulting structural coloration phenomenon.

Spatial features: Ref. [11] claimed that if the dimension of the microsphere is sufficiently large, one should be able to exclude the interference that occurs between two rays from the opposite edges of the sphere and therefore observe the multi-bouncing TIR interference pattern exclusively. However, according to the doublet experimental estimation in Section S5, the spatial coherent areas of light sources can be much larger than microspheres used in Refs. [11,14,20]. The multi-bouncing interference is not an exclusive mechanism in this MCI. As shown in Section S6, we first employed two white light sources to illuminate the 10 µm PS sample and observed nearly identical multiple rainbow patterns (Fig. **S8a**) that can be reproduced with modeling by using our proposed complete angle-dependent interference mechanism (Fig. 2E). More importantly, the assumption made within Ref. [11] can easily be broken when lasers with long coherent lengths are employed in the experiment. As shown in Figs. S8b-S8d, we used three lasers as the incident light source and measured the monochromatic reflection patterns that were produced by our MCIs. Intriguingly, these measured patterns agree well with the modeled patterns that use the complete angle-dependent interference mechanism. It is these monochromatic rings that result in the multi-concentric rainbow rings observed under white light illumination. Therefore, the multi-bouncing TIR picture proposed by Ref. [11] is not the exclusive mechanism for these 10 µm PS MCI samples.

In order to reveal the relationship between the spatial coherent length of the light source and the sphere size, we fabricated a new hetero-interface MCI structure using larger PS microspheres (42 µm) partially embedded in the tape (Fig. 3A). Due to the identical refractive index distribution, ray tracing modeling revealed that TIR bouncing was only possible with modes of m = 2, and m = 3. Here, we first illuminated the MCI with a coherent laser while changing the sample-board distance, h (see Supporting Video S2 for an experimental demo under the illumination of a laser at 405 nm, and an example observed at a distance of 32 cm in the upper half panel in Fig. 3B): as h increases, high frequency rings can be observed on top of the low frequency rings. These combined high-and-low frequency spatial patterns can also be observed under the illumination of other visible lasers (see upper half panels in Fig. 3C,D for lasers at 534 nm and 632 nm, respectively, at a distance of 32 cm). To interpret this mechanism, we employed the multi-bouncing TIR picture to model the spatial beam patterns in Fig. 3E-G, showing the low frequency pattern only. One can see that this mechanism cannot explain the high frequency multi-ring pattern observed in our experiment. When we further considered the interference of rays from the opposite edges of the sphere in the modeling (as shown in the lower half panels in Fig. 3B-D), the high frequency rings on top of the low frequency patterns were obtained, agreeing very well with the measured data in the upper half panels. Therefore, both mechanisms (i.e., the complete angle dependent interference) are responsible for this intriguing observation, which is different from both the 'exclusive' single-sided multi-bouncing TIR interference mechanism proposed by Refs. [11] and [20], and the air gap interference mechanism proposed by Ref. [14].

Next, we employed a partially coherent light source (e.g. a laser-driven white light source) to illuminate the MCI sample and

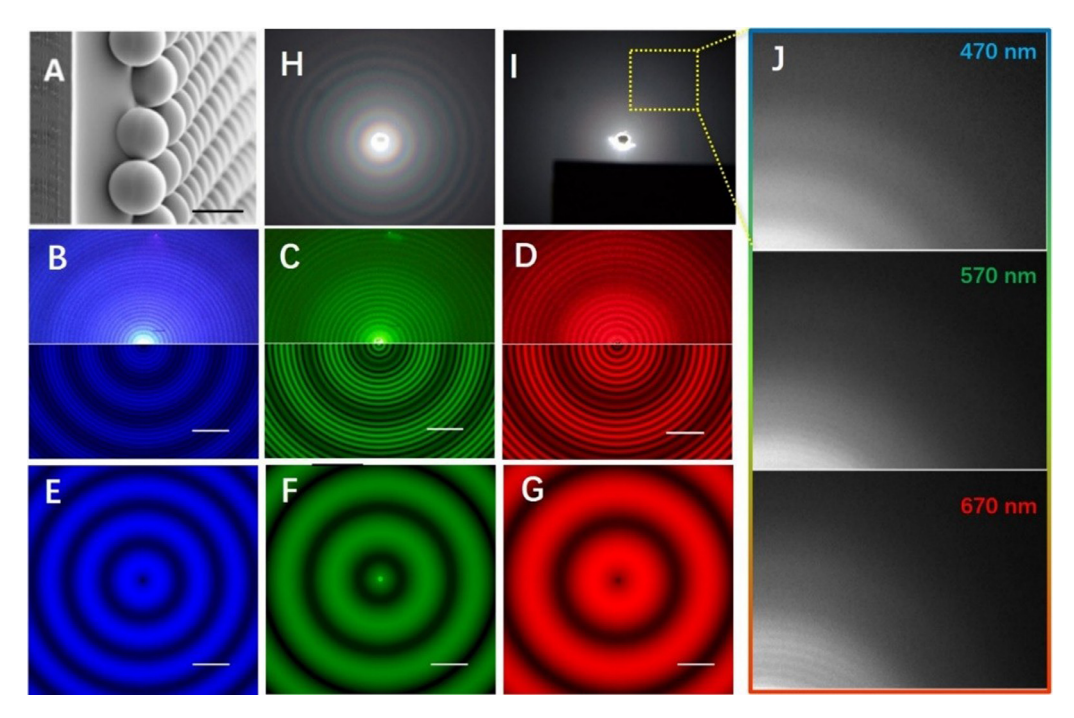


**Fig. 3.** Spatial patterns of the MCI. (A) SEM image of the embedded 42  $\mu$ m microspheres within the sticky polyacrylate tape (scale bar = 40  $\mu$ m). (B-D) Upper panels: Measured reflected patterns at a distance h=32 cm when illuminated with a laser at a wavelength of (B) 405 nm, (C) 534 nm, and (D) 632 nm. Lower panels: Modeled patterns that consider the complete angle-dependent superposition. (E-G) Modeled patterns that utilize the multi-bouncing TIR superposition only at wavelengths of (E) 405 nm, (F) 534 nm, and (G) 632 nm, respectively. Scale bars in Fig. 4(B-G) indicate 3 cm. (H,I) Photos of the reflected pattern at a distance of (H) h = 32 cm and (I) h = 9.5 cm, respectively, when illuminated by a laser-driven white light source. (J) Measured grey-scale images of reflected patterns at a distance of 9.5 cm when illuminated by narrow band wavelengths at 470 nm, 570 nm and 670 nm, respectively.

observed a similar multi-ring pattern at a distance of h=32.0 cm (Fig. 3H). However, when the distance was adjusted, and the sample brought closer to the board, the high frequency rings became invisible (as shown in Fig. 3I, when h=9.5 cm). Instead, a blurred single rainbow was observed, which is similar to the results reported in Refs. [11,20]. However, this observation still cannot rule out the interference of rays from opposite edges of the sphere. There are two possibilities responsible for the disappearance of the high-frequency rainbow (Section S7): i.e., the spatial feature is not resolvable at this distance, and/or the spatial coherent length of the incident light is smaller than the microsphere (i.e., the exclusive multi-bouncing mechanism reported by Ref. [11]). Since all monochromatic rings overlap with each other under white light illumination, it is necessary to reveal the actual underlying physics using narrow band incident light.

Considering the analytical equation of the spatial coherent area (i.e.,  $\Delta A \sim \frac{l_D^2 \tilde{\lambda}^2}{S}$ ), one can finely tune the spatial coherent length of the incident light by controlling  $\bar{\lambda}$ . As shown by the left panel in Fig. 3J, the central wavelength of the incident light is tuned by a liquid crystal filter with a bandwidth of  $\sim 7$  nm from 470 nm (the top panel), to 670 nm (the bottom panel), corresponding to a coherent length very similar to the microsphere (i.e. 42 µm). Specifically, one can see the low-frequency pattern only at the wavelength of 470 nm as shown by the top panel in Fig. 3J. According to the numerical modeling, the spatial feature of the high-frequency pattern is  $\sim$  1.33 mm at this distance of h = 9.5 cm, which is resolvable by naked eyes (Fig. S9). Therefore, the disappearance of the interference pattern under the illumination of the less coherent light source can be safely attributed to the insufficient spatial coherent length at the incident wavelength of 470 nm. On the other hand, one can see high-frequency features when the filter is tuned to 670 nm (i.e. the bottom panel in Fig. 3J). Remarkably, the angle range of these high-frequency patterns is up to  $\sim 39.0^{\circ}$ , agreeing well with the theoretical prediction in Fig. 2A. Therefore, careful

manipulation of the spatial coherent length of the light source, microsphere dimension and illumination/observation angles can result in different interference phenomena in the reflected light, corresponding to different color changing features from a given MCI structure. For instance, under the illumination at large incident angles of 40°-50° (e.g. Refs. [11] and [20]), the exclusive multibouncing mechanism is possible when the incident light cannot be coupled into the sphere from both edges simultaneously, which is not due to an insufficient spatial coherent length. On the other hand, when considering the rapid color flickering phenomenon observed in large scale passive "smart" traffic signs in the far-field reported by Ref. [14], the spatial coherent length of a car's headlights is much greater than the diameter of the microsphere used [> 250  $\mu$ m, with  $L_D = 100$  m (See Section S5)], which means that the spatial interference introduced by rays at opposite edges of the sphere is the major color generation mechanism.

To show the angle dependence in different spatial angle ranges, here we observed the real MCI sample (made by 10 µm PS spheres) and its mirror image simultaneously, as shown in Fig. 4A (see experimental details in Sec. S8). A white light source is used to illuminate the sample near the normal direction at a distance of  $\sim$ 0.74 m. The observation angle,  $\theta$ , is tuned from  $\sim$ 3° to  $\sim$ 16° to capture the reflection image of the MCI sample (Fig. 4B). The corresponding observation angle of its mirror image,  $\alpha$  is from  $\sim$ 16° to 28°. Intriguingly, the color of the real sample changes frequently within the small observation angle range (the lower panel in Fig. 4B), while the mirror image color stays relatively consistent in the relatively large observation angle range (the upper panel in Fig. 4B). The red, green and blue (RGB) pixel data of these images was extracted in order to plot color points in the CIE chart (Fig. 4C). One can see that the real sample observed within 3° to  $\sim 16^{\circ}$  covers a wider color range in the CIE chart. In order to quantitatively measure the color change of the MCI sample, we plotted the angle-dependent Euclidean distances (a parameter used to

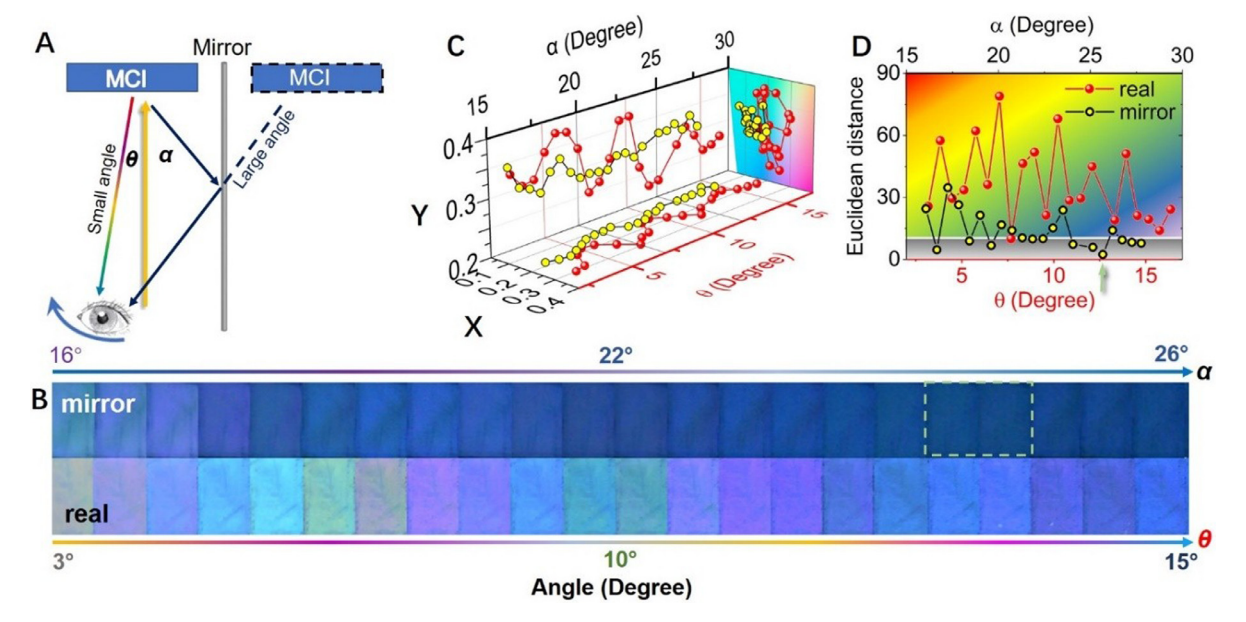


**Fig. 4.** Direct observation of the angle dependent reflection of the MCI pixel array. (A) Schematic illustration of the mirror image setup (not to the actual scale). As the observation angle increases, the color of the MCI changes. (B) Reflection images of the MCI sample at  $\theta$  of 3°~16° with corresponding mirror images at α of 16°~28°. (C) The angle-dependent CIE points of the MCI sample (red spheres) and its mirror image (yellow spheres). (D) The angle-dependent Euclidean distances of the real sample and its mirror images [i.e.,  $E = \sqrt{(R_1 - R_2)^2 + (G_1 - G_2)^2 + (B_1 - B_2)^2}$ , here R, G, B represent the values of Red, Green and Blue codes, respectively] (For interpretation of the references to color in this figure legend, the reader is referred to the web version of this article.).

quantify color differences [22]) of the real sample and its mirror image, which are shown in Fig. 4D. According to the standard set by the CIE in 1976 [22], when the Euclidean distance, E, between 2 color points, is below 1, the color change is imperceptible to the human eye. When the value is between 2 and 10 (i.e.,  $16^{\circ}\sim28^{\circ}$  region for the mirror sample, see the gray shaded region in Fig. 4D), the color change becomes barely visible. One can see that most Euclidean distances of the real images are larger than those of the mirror images. In particular, the smallest E is ~2.45 for the mirror image at  $\alpha{\approx}25^{\circ}$  (see the two images highlighted by the dotted square in Fig. 4B and the arrow in Fig. 4D). At higher values (the rainbow shaded region in Fig. 4D), the difference becomes more striking with larger E. This quantitative color analysis of the MCI sample validates the unique angle dependence of its reflection feature. Building upon this accurate understanding of the new coloration mechanism from these MCI structures, we will demonstrate the reflective display concept by introducing actively tunable

Actively tunable reflective displays: To realize color changing displays, one will need active strategies to change the reflection conditions of MCI pixels and arrays. For instance, dielectric elastomer actuators (DEA) have been developed using electroactive polymers with promising applications for advanced mechanical systems and robotics [23-25]. Here we first integrated the MCI structure with a DEA pixel (Fig. 5A, see fabrication details of a portable DEA system in Sec. S9a). As shown in Fig. 5B, the shape of the DEA can be tuned to control the reflection angle, resulting in actively tunable colors for the MCI under a fixed white light illumination. Moreover, MCIs are particularly suitable for large scale pixelated reflective displays. For instance, the flip-disc or flip-dot display is an electromechanical matrix technology developed for large signs (e.g. outdoor traffic and advertisement boards) under external light illumination. By integrating the MCIs onto the pixels of this largescale display, color changing information will be enabled under directional illumination and at varying observation angles. As illustrated in Fig. 5C, we manually tuned the pixel array to demonstrate this simple colorful display concept using a white light un-

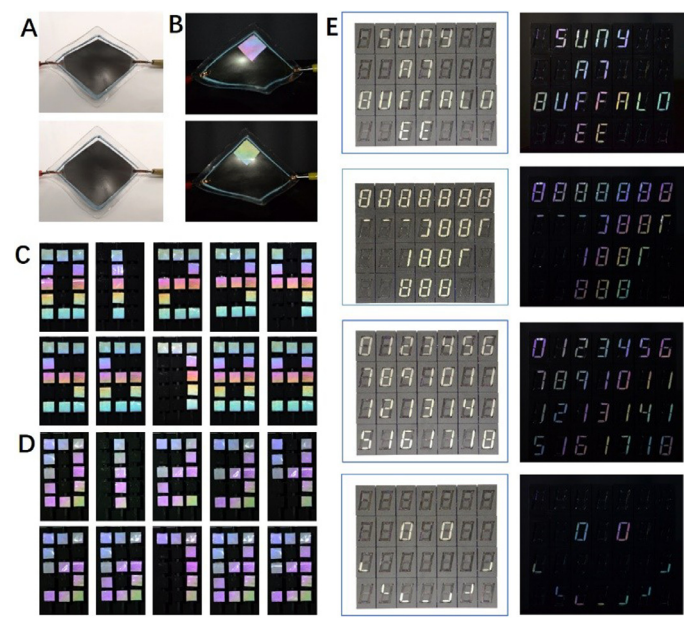


**Fig. 5.** Actively tunable MCI displays. (A) Photos of a DEA device with tunable shapes. (B) Photos of the tunable color from the MCI on a DEA under a fixed white light illumination (at a normal incident angle and an observation angle of  $\sim^3$ '). (C,D) A demo of a manually tunable pixel array display observed at the observation angle of (C)  $\sim^3$ ', and (D)  $12^\circ$ , respectively, under the illumination of a normal incident white light. (E) Integration with a 7  $\times$  4 flip-dot module (ALFAZETA ®) for colorful display demos.

der normal incidence. *Supporting Video S3* shows the color changing pattern at different observation angles. In particular, when the observation angle was changed to  $\sim 12^{\circ}$ , the colors changed significantly as shown in Fig. 5D. Intriguingly, by integrating the MCI structures with a commercial  $7 \times 4$  flip-dot module (see details in **Sec. S9b**), different patterns can easily be controlled via algorithms (Fig. 5E). Under room light illumination, one can see that



**Fig. 6.** Visible and IR reflective signs under different light illumination conditions. (a) Proposed implementation of MCI in LiDAR technology for simultaneous visible and IR imaging and pattern recognition. (b) A 3  $\times$  3 block of PS microsphere samples with various diameters (4, 5, and 6 μm in top row, 7, 8, and 10 μm in middle row, and 15, 22, and 39 μm on the bottom row). The observation distance is 20 cm. (c) Experimental setup used to demonstrate effectiveness of the MCI signs for indoor LIDAR application. (d) Simultaneous visible, IR and distance mapping images observed by the LiDAR camera at the normal direction and the distance of  $\sim$ 0.37 m. (e) Corresponding visible and IR images of the MCI sign observed at three different angles of 5°, 20° and 35°, respectively (For interpretation of the references to color in this figure, the reader is referred to the web version of this article.).

the module shows black-and-white information only. In particular, all elements on each pixel can still be seen clearly when they are off (i.e., black patterns in the left row in Fig. 5E). In contrast, in the low light illumination condition at the normal direction, vivid color information was obtained in the reflection side, demonstrating a new reflective display for darkrooms and nighttime outdoor applications (the right row in Fig. 5E, see more display examples in *Supporting Video S4*, and *Fig. S11*). The black patterns were less observable due to the dark background, resulting in a dark-field color pattern with a visibly better contrast than the one observed under room light illumination. Furthermore, this concept is fully amenable to digital micromirror devices [26,27] and is promising to create new microscale reflective display applications to address current challenges faced by autopilot/autonomous systems.

Smart signs for LIDAR systems: In Ref. [7], various large scales patterns were developed for smart nighttime traffic signs. When the traffic sign was illuminated by the headlight of a moving car, the slowly moving passengers observed a rapid color change with no active electronic control circuits (i.e. iridescence). In contrast, the driver in the car saw a stable sign since the observer (i.e., the driver) and the headlight move together (i.e. retroreflection). Here we will further demonstrate an application by combining these two phenomena from the visible to near infrared regimes for future autopilot/autonomous applications. As illustrated in Fig. 6a, current autopilot systems mainly rely on LIDAR systems to image the surrounding environment, and recognize traffic situations using infrared (IR) lasers. However, IR sensing/imaging cannot accurately recognize traffic signs. The mainstream solution is to use visible CCD cameras combined with artificial intelligence algorithms for visual pattern recognition and classification. Unfortunately, this

combined solution is suffering from robust physical-world attacks [28,29]: for instance, when a regular STOP sign was perturbed with a predesigned mask, the algorithms interpreted this sign to be a speed limit sign of 45 miles/hour [30], which can cause the vehicle to crash. Recently, we have witnessed many traffic accidents due to the weakness of current LIDARs in autopilot systems [31–33]. The major issue is that conventional traffic signs contain limited information for visual classification. This technical challenge can be largely addressed by the MCI patterns since the concentric multiring phenomenon can be observed in both visible (Figs. 1 and 3) and IR regimes (Fig. S12). Intriguingly, in this autopilot application, the retroreflection and iridescent features of the MCI structure can introduce a unique two-fold benefit: i.e. the IR laser of the LIDAR system will enable the angle-independent retroreflection response, while the visible imaging portion that relies on external light sources will experience an angle-dependent color changing signal that allows for visible pattern recognition.

As shown in Fig. 6b, a 3  $\times$  3 square array using 9 different PS spheres with diameters ranging from 5 to 42  $\mu$ m were fabricated, as labeled on each unit. Under a fixed white light illumination (e.g. illuminated by a streetlight at a fixed angle) and a changing observation angle (i.e. the driver's view), one can observe vivid colorful patterns from these 9 units. As an example, when one concentrates on the 10  $\mu$ m PS MCI sample, the color changes from purple to blue and green as the observation angle changes within the range of 0° to 35° (Fig. 6b). When illuminated by a single wavelength from the car (as is the case with a LIDAR camera), the IR imaging condition is very different from the visible one: i.e. the illumination source and the camera will move together, providing for a stable, retroreflective signal to be observed. Therefore,

the simultaneous iridescence and retroreflection feature enabled by the MCI structure can introduce a new signal that can be integrated with future reflective signs with extra signals/information for emerging autopilot and robotic systems. As illustrated in Fig. 6c, we fabricated a STOP sign using 7 µm (top and bottom parts) and 15 µm PS spheres (the central letters), and employed a commercial high-resolution LIDAR camera for indoor distance characterization to capture the image of the test sign. In this experiment, we employed a portable white light source to illuminate the test sign to mimic an aligned streetlight for traffic signs. As the observation angle of the LIDAR camera changes (i.e. the LIDAR camera is moving with the car), one can obtain visible, IR and distance mapping simultaneously (see Fig. 6d for three images at the normal direction, and Supporting Video S5 for visible, IR and distance mapping videos captured simultaneously at a distance of  $\sim$ 0.37 m by the LIDAR camera). Intriguingly, the IR reflection intensities of the MCI pattern under the illumination of a laser with a wavelength of 860 nm are obviously stronger than the background paper (see the central panel of Fig. 6d), indicating that the MCI structure can be used as the building block for future signs designed for IR imaging and pattern recognition. One can see that the color of the MCI sign changes with different observation angles (Fig. 6e), which is in stark contrast of the standard retroreflective signs (e.g. traffic signs). On the other hand, Fig. 6d shows that the LIDAR camera can clearly recognize the MCI sign with the IR camera, and build the appropriate depth map (right panel in Fig. 6d). Importantly, due to the retroreflective feature of the MCI reported in our earlier work [14] (i.e. the incident angle and the observation angle are moving together), the IR image shows a strong and stable pattern at different angles ( $\sim$ 5° in the left panel,  $\sim$ 20° in the middle panel, and  ${\sim}35^{\circ}$  in the right panel of Fig. 6e). Therefore, the pattern recognition can be significantly improved due to the simultaneous visible color change, and stable IR image.

## 3. Conclusion

In conclusion, the actual optical interference mechanism of the MCI structure is clarified with systematic experimental characterization and numerical modeling. It was revealed that different interference mechanisms exist in the reflection from the MCI structure with different angle dependence features. In particular, the output beams from opposite edges of the microsphere structure will interfere with each other and result in a high-frequency multiple rainbow ring pattern in the far-field, which is the key mechanism of the new coloration microstructure but was neglected by previous works. The concentric interference ring patterns were analyzed and validated using coherent and semi-coherent light sources. Building upon these remarkable colorful patterns, the application of actively tunable reflective displays was demonstrated using DEA and flip-disc concepts, which have the potential to deliver color changing visible patterns under the illumination of weak external broadband light sources. Intriguingly, we also demonstrated a potential application with the integration of our MCI structure and infrared imaging in the form of LIDAR depth mapping. The dual visible color changing and infrared stability can potentially improve the traffic recognition capabilities of current autopilot and autonomous driving systems. The implementation of this large-scale MCI holds promising new avenues for future traffic safety signs, optical sensing platforms, anti-counterfeiting tags, advanced cameras [34], light emitting devices [35], display technologies [36] and robotic vision [37].

## 4. Methods

MCI fabrication: We followed the manufacturing process reported in Ref. [14] to fabricate large scale MCI structures: A mono-

layer of closely packed PS microspheres was first assembled on a substrate using colloidal assembly methods [38]. The homogenous microsphere solution is placed into a beaker, and the excess solution is boiled off on a hotplate at 100 °C for 15 min. The microsphere particles are transferred onto a thin slice of PDMS, and remain unordered. A second piece of PDMS is used to rub the spheres, creating an ordered monolayer on the bottom PDMS layer. Once a sufficient monolayer is formed, a transparent piece of tape is placed on top of the spheres, sticky side down. Then, the microsphere array was transferred onto the sticky side of a transparent tape by pressing the tape onto the microsphere array and subsequently peeling the microspheres off the substrate with the tape. After applying a controlled pressure on the tape, the microspheres can be pushed into the tape layer and form the MCI shown in Figs. 1B and 3A.

Optical characterization: A laser-driven white light source (EQ99-XFC, ENERGETIQ ®) was employed to illuminate the MCI sample in Fig. 1. The reflection spectra were characterized using a fiber-based spectrometer (Ocean Optics Inc Jaz). Three lasers were used to obtain the far field reflection patterns of the MCI structure, with average powers of 10 mW for 405 nm, 34 mW for 534 nm, and 3 mW for 632 nm. Refractive indices of the tape were measured using a digital refractometer (Reichert Brix/RI-Check Refractometer).

The coherent length of both the laser-driven white light source, and halogen lamp (Olympus U-LH100L), was measured on an inverted optical microscope (Olympus IX-81). Two doublets with varying edge-to-edge distances (94 µm and 144 µm) were fabricated using focused-ion-beam (FIB, Carl Zeiss Auriga CrossBeam) milling on 300 nm thick silver that was deposited onto a glass slide via electron-beam evaporation (Kurt J. Lesker PRO Line PVD 75). A liquid crystal tunable filter (CRI Varispec VIS2-07) was used to illuminate the doublets at a specific wavelength for further characterization. All pictures were recorded using a Hamamatsu digital camera (C8484-03G02).

For the NIR ring characterizations, an 808 nm laser (ADR-1805 laser diode T7-Type) was used to illuminate the 10  $\mu m$  PS sample. A black and white CCD camera (Point Grey CCD camera; model: CMLN-13S2M-CS) was used to observe the NIR rings. When imaging the 3  $\times$  3 PS array, and stop sign, a commercial indoor LiDAR camera (Intel® RealSenseTM LiDAR Camera L515) was used [39]. The white light used in this experiment was a handheld flashlight (Fenix E12).

Numerical modeling: Ray tracing modeling was performed using the Ray Optics Module of COMSOL Multiphysics ®. In this work, the MCI structure was illuminated by normal incident rays. The properties of each output ray, including the propagation direction, intensity, phase, wavefront curvature, and the escaping point from the tape to air, can be determined using ray tracing simulation. If the reflected light pattern is observed at far distance (i.e., much larger than the diameter of the sphere), the far-field distribution can be calculated. Based on results of the output ray parameters from the ray tracing simulation, the spectral and spatial characteristics of the reflected field in Figs. 2 and 3 were modeled by considering the interference of exit rays propagating along the same directions. An example of the calculation algorithm package is available online for readers to further validate the proposed theoretical procedure: https://github.com/nabla2020/ multiple\_concentric\_rainbow

#### **Declaration of Competing Interest**

J.Z, H.S., W.F., L.W. and Q.G. are named as inventors on a patent application pertaining to this work (Patent number: 10,838,119). The authors declare that they have no personal relationships that could have appeared to influence the work reported in this paper.

#### Acknowledgments

The authors appreciate the helpful discussion with Dr. Xiuling Li from UIUC. This work was partially supported by the National Science Foundation (grand no. ECCS-1807463 and the EPMD program of 'Microscale concave interfaces for structural reflective coloration').

## Supplementary materials

Supplementary material associated with this article can be found, in the online version, at doi:10.1016/j.apmt.2021.101146.

#### References

- B. Comiskey, J.D. Albert, H. Yoshizawa, J. Jacobson, An electrophoretic ink for all-printed reflective electronic displays, Nature 394 (1998) 253–255.
- [2] R.A. Hayes, B.J. Feenstra, Video-speed electronic paper based on electrowetting, Nature 425 (2003) 383–385.
- [3] Simonite, T. E-reader display shows vibrant color video, <a href="https://www.technologyreview.com/2011/11/15/189719/e-reader-display-shows-vibrant-color-video/">https://www.technologyreview.com/2011/11/15/189719/e-reader-display-shows-vibrant-color-video/</a> (2011).
- [4] E. Downing, L. Hesselink, J. Ralston, R. Macfarlane, A three-color, solid-state, three-dimensional display, Science 273 (1996) 1185.
- [5] N.R. Council, Virtual Reality: Scientific and Technological Challenges, The National Academies Press, 1995.
- [6] T. Someya, Z. Bao, G.G. Malliaras, The rise of plastic bioelectronics, Nature 540 (2016) 379–385.
- [7] Carlowicz, M. New night lights maps open up possible real-time applications, <a href="https://www.nasa.gov/feature/goddard/2017/new-night-lights-maps-open-up-possible-real-time-applications">https://www.nasa.gov/feature/goddard/2017/new-night-lights-maps-open-up-possible-real-time-applications</a>
- [8] A. Irwin, The dark side of light, Nature 553 (2018) 4.
- [9] E. Pennisi, Light pollution may promote the spread of West Nile virus, Science (2018), doi:10.1126/science.aas9594.
- [10] Q. Li, et al., Light at night and breast cancer risk: results from a population-based case-control study in Connecticut, USA, Cancer Causes Control 21 (2010) 2281–2285.
- [11] A.E. Goodling, et al., Colouration by total internal reflection and interference at microscale concave interfaces, Nature 566 (2019) 523–527.
- [12] C.A.C. Chazot, et al., Luminescent surfaces with tailored angular emission for compact dark-field imaging devices, Nature Photonics 14 (2020) 310–315.
- [13] K. Chau, Colour from colourless droplets, Nature 566 (2019) 2.
- [14] W. Fan, et al., Iridescence-controlled and flexibly tunable retroreflective structural color film for smart displays, Sci. Adv. 5 (2019) eaaw8755.
- [15] Y. Qi, et al., Retroreflection and wettability controlled smart indicator based on responsive bilayer photonic crystals for traffic warning, Adv. Opt. Mater. 8 (2020) 2001367.

- [16] J.A. Adam, The mathematical physics of rainbows and glories, Phys. Rep. 356 (2002) 229–365.
- [17] A. Haubmann, Rainbows in nature: recent advances in observation and theory, Eur. J. Phys. 37 (2016) 063001.
- [18] G. Wyszecki, W.S. Stiles, Color Science: Concepts and Methods, Quantitative Data and Formulas, Wiley, 1967.
- [19] LLC, C. Polystyrene Spheres (PS), <a href="https://www.cospheric.com/psms-1-07-g-cc-highly-spherical-thermoplastic-biocompatible-microparticles.aspx">https://www.cospheric.com/psms-1-07-g-cc-highly-spherical-thermoplastic-biocompatible-microparticles.aspx</a>(2020).
- [20] A.E. Goodling, S. Nagelberg, M. Kolle, L.D. Zarzar, Tunable and responsive structural color from polymeric microstructured surfaces enabled by interference of totally internally reflected light, ACS Mater. Lett. 2 (2020) 754–763.
- [21] L. Mandel, E. Wolf, Optical Coherence and Quantum Optics, Cambridge University Press, 1995.
- [22] G. Sharma, R. Bala, Digital Color Imaging handbook (2003).
- [23] A. O'Halloran, F. O'Malley, P. McHugh, A review on dielectric elastomer actuators, technology, applications, and challenges, J. Appl. Phys. 104 (2008) 071101.
- [24] C. Keplinger, et al., Stretchable, transparent, ionic conductors, Science 341 (2013) 984.
- [25] M. Duduta, E. Hajiesmaili, H. Zhao, R.J. Wood, D.R. Clarke, Realizing the potential of dielectric elastomer artificial muscles, Proceedings of the National Academy of Sciences 116 (2019) 2476.
- [26] Y.X. Ren, R.D. Lu, L. Gong, Tailoring light with a digital micromirror device, Ann. der Phys. 527 (2015) 447–470.
- [27] T. Yoon, C.S. Kim, K. Kim, J.r. Choi, Emerging applications of digital micromirror devices in biophotonic fields, Opt. Laser Technol. 104 (2018) 17–25.
- [28] D. Heaven, Why deep-learning Als are so easy to fool, Nature 574 (2019)
- [29] M. Taddeo, T. McCutcheon, L Floridi, Trusting artificial intelligence in cybersecurity is a double-edged sword, Nat. Mach. Intell. 1 (2019) 557–560.
- [30] K. Eykholt, I. Eytimov, E. Fernandes, Bo. Li, A. Rahmati, C. Xiao, A. Prakash, T. Kohno, D. Song, Robust physical-world attacks on deep learning visual classification, in: Proceedings of the CVPR, 2018.
- [31] Been, R., Levin, A., Another self-driving crash highlights risks of sharing road with robots, https://www.newequipment.com/technology-innovations/ article/22059585/another-selfdriving-crash-highlights-risks-of-sharing-roadwith-robots (2017)
- [32] White, J., California police investigating fatal Tesla crash, https://www.reuters.com/article/us-tesla-crash/california-police-investigating-fatal-tesla-crash-idUSKBN2CN026 (2021)
- [33] Uber in fatal crash had safety flaws say US investigators, https://www.bbc.com/ news/business-50312340 (2018)
- [34] Y. Song, et al., Digital cameras with designs inspired by the arthropod eye, Nature 497 (2013) 95.
- [35] Y. Nishijima, et al., Lasing with well-defined cavity modes in dye-infiltrated silica inverse opals, Opt. Express 17 (2009) 2976.
- [36] D.Y. Kim, M.J. Kim, G. Sung, J.Y. Sun, Stretchable and reflective displays: materials, technologies and strategies, Nano Converg. 6 (2019) 21.
- [37] Xie, M. Robot vision: a holistic view. (2005).
- [38] C. Park, et al., Quick, large-area assembly of a single-crystal monolayer of spherical particles by unidirectional rubbing, Adv. Mater. 26 (2014) 4633–4638.
- [39] https://docs.rs-online.com/f31c/A700000006942953.pdf.